

# LAMOST J045019.27+394758.7, with peculiar abundances of N, Na, V, Zn, is possibly a Sculptor dwarf galaxy escapee <sup>★</sup>

Meenakshi Purandardas<sup>1,2</sup>, Aruna Goswami<sup>1,3</sup> †, J. Shejeelammal<sup>1</sup>, Mayani Sonamben<sup>1,3</sup>, Ganesh Pawar<sup>4</sup>, David Mkrtichian<sup>5</sup>, Vijayakumar H. Doddamani<sup>2</sup>, Santosh Joshi<sup>4</sup>

<sup>1</sup>Indian Institute of Astrophysics, Koramangala, Bangalore 560034, India;

<sup>2</sup>Department of physics, Bangalore university, Jnana Bharathi Campus, Karnataka 560056, India

<sup>3</sup>Institute of Frontier Science and Application, Bangalore, Karnataka, India

<sup>4</sup>Aryabhata Research Institute of Observational Sciences (ARIES), Manora Peak, Nainital-263001, Uttarakhand, India.

<sup>5</sup>National Astronomical Research Institute of Thailand (NARIT) 260 Moo 4, T. Donkaew, A. Maerim, Chiangmai, 50180 Thailand

Accepted 2022 April 22. Received 2022 April 22; in original form 2021 September 14

## ABSTRACT

We present the results of the high-resolution ( $R \sim 60,000$ ) spectroscopic analysis of the star LAMOSTJ045019.27+394758.7 (hereafter J045) from the list of carbon stars of LAMOST DR2. From our analysis, we find that J045 does not exhibit the spectral characteristics of carbon stars. It is found to be a metal-poor ( $[Fe/H] = -1.05$ ) giant that shows very unusual elemental abundances, particularly for N, Na, V, and Zn. J045 shows  $\alpha$ -elements (Mg, Si, Ca) with near-solar values ( $\langle [\alpha/Fe] \rangle = 0.09$ ) in contrast to Galactic stars that show  $[\alpha/Fe]$  in the range 0.2 to 0.3 dex. In J045, Sc and Ti are under abundant with  $[X/Fe] \leq -0.25$ . Vanadium gives  $[V/Fe] = 0.51$  and zinc is under-abundant with  $[Zn/Fe] = -0.62$ . The object exhibits near-solar abundances for Sr, Y, Ba, Pr, and Sm. The La is marginally enhanced, and Ce and Nd are marginally under-abundant in J045. With  $[Ba/Eu] = -0.38$ , the object falls into the category of neutron-capture rich r-I stars. The estimated abundances of various elements show that the observed abundance pattern is not compatible with the abundances characteristic of Galactic metal-poor stars but matches quite closely with the abundance pattern of Sculptor Dwarf galaxy stars of similar metallicity. Based on the above observational evidences, we suggest that the object is a possible Sculptor Dwarf Galaxy escapee.

**Key words:** stars: abundances - stars: carbon stars - stars: atmospheres - stars: metal-poor

## 1 INTRODUCTION

Carbon stars are a special class of objects characterised by strong molecular bands of carbon such as C<sub>2</sub>, CH and CN in their spectra. Many surveys were conducted to explore carbon stars such as the First Byurakan Spectral Sky Survey (Gigoyan et al. 1998), infrared objective-prism surveys (Alksnis et al. 2001, Automatic Plate Measuring survey (Totten & Irwin 1998; Ibata et al. 2001), and references therein), and the Large Sky Area Multi-Object Fibre Spectroscopic Telescope (LAMOST, Wu et al. 2011; Bai et al. 2016; Ji et al. 2016). Many studies have shown that a large fraction of iron-deficient stars exhibit enhancement of carbon as well as neutron-capture elements and are the ideal candidates to study the mechanism(s) that produce these elements. The chemical peculiarity of these objects promoted many spectroscopic studies of this group. One of our primary goals is therefore to explore carbon enhanced stars with signatures of enhanced abundance of heavy elements from large surveys for conducting such studies.

Following the low-resolution spectroscopic analysis, Goswami (2005); Goswami et al. (2007); Goswami et al. (2010), identified a substantial fraction ( $\sim 30\%$ ) of CH stars from the list of faint high-latitude carbon stars of Christlieb et al. (2001). Follow-up detailed

chemical analysis of some of these objects have shown many of them to be carbon-enhanced metal-poor (CEMP) stars in a metallicity range  $[Fe/H] < -1$ , comprising of CEMP-r/s, CEMP-s and CEMP-no stars (Goswami et al. 2006; Purandardas et al. 2019b; Goswami et al. 2021; Purandardas & Goswami 2021a). Ji et al. (2016) could identify 894 carbon stars from LAMOST DR2, from the measurement of the line indices of carbon molecular lines using spectra with  $R \sim 1800$ , and  $S/N > 10$ , and classified them into various spectral sub-classes such as C-N, C-R, and C-H. We performed a detailed chemical analysis for a few objects from this list and showed that the estimated abundances of the CEMP-r/s star LAMOSTJ151003.74+305407.3 (hereafter J151) could be well explained by the model yields ( $[X/Fe]$ ) of i-process nucleosynthesis of heavy elements, and LAMOSTJ091608.81+230734.6 (hereafter J091) was identified as a CH giant (Shejeelammal et al. 2021). A parametric model based analysis have also shown that the model yields ( $[X/Fe]$ ) of i-process nucleosynthesis of heavy elements could well explain the estimated abundance patterns of J151. The estimated neutron-density-dependent  $[Rb/Zr]$  ratio confirmed former low-mass asymptotic giant branch companions for these two objects. Our kinematic analysis have shown that J151 is a halo object and J091 belongs to the disk population (Shejeelammal et al. 2021).

We report here the results based on the high-resolution abundance analysis of another object J045 from Ji et al. (2016) which is

<sup>★</sup> Based on data collected using HCT/HESP

† E-mail: aruna@iiap.res.in

classified as a carbon star with no identifiable sub-type. Xiang et al. (2019) derived the atmospheric parameters and elemental abundances for O, C, N, Mg, Na, Si, Ti, Ca, Cr, Co, Mn, Ni, and Ba based on low-resolution ( $R \sim 1800$ ) spectroscopic analysis and using data driven models. Based on near-infrared (15140-16940 Å) spectroscopy using a spectra at a resolution of  $R \sim 22,500$ , Jonsson et al. (2020) determined the atmospheric parameters as well as these elemental abundances except for Ba using APOGEE Stellar Parameter and Chemical Abundance pipeline (ASPCAP). While Xiang et al. (2019) estimated the atmospheric parameters  $T_{\text{eff}}$ ,  $\log g$ , microturbulent velocity  $\zeta$ , and metallicity  $[\text{Fe}/\text{H}]$  for this object as (4627 K, 2.26, 0.72 km s<sup>-1</sup>, -0.90), these estimates derived by Jönsson et al. (2020) are respectively (4250 K, 1.00, 1.55 km s<sup>-1</sup>, -0.50). The large difference in the estimates of the atmospheric parameters by these two groups have prompted us to re-visit this object. Although some of the aspects were discussed in these two studies, in this work, the results from a high-resolution spectroscopic analysis ( $R \sim 60,000$ ) of this object is presented for the first time. In addition to the elements for which the abundances are available in these two studies, we have determined the abundances for a few more elements such as Eu, Sm, Nd, Pr, La, Sr, Y, and Zn. Our analysis, however, shows that this object does not exhibit the spectral properties of carbon stars. From a visual inspection of its spectrum, the molecular bands due to carbon are found to be very weak, and also enhanced signature of neutron-capture elements were absent in the spectrum. We find a metallicity  $[\text{Fe}/\text{H}] = -1.05$  for this object with elemental abundances that are quite unusual from that expected for Galactic metal-poor stars of similar metallicity. The observed abundance pattern is however found to be compatible with the abundance patterns observed in Sculptor Dwarf galaxy stars, indicating that the object J045 is possibly a Sculptor Dwarf Galaxy escapee. We have also examined for signatures of any internal mixing in this object using <sup>12</sup>C/<sup>13</sup>C and  $[\text{C}/\text{N}]$  ratios that were not discussed in the previous works.

The paper is arranged as follows: Section 2 discusses observation and data reduction. Estimation of stellar atmospheric parameters, mass, and age determination are discussed in Section 3. A discussion on the determination of abundances is presented in Section 4. Uncertainty in the abundance estimates is discussed in Section 5. Results of the TESS photometry for the programme star is presented in Section 6. Results obtained from the kinematic analysis are discussed in Section 7. A discussion on the abundance analysis is given in Section 8 and the conclusions are presented in Section 9.

## 2 OBSERVATIONS AND DATA REDUCTION

The object J045 is taken from the sample of carbon stars listed in LAMOST DR2 (Ji et al. 2016). The high-resolution ( $R \sim 60,000$ ) spectrum of the object is obtained from the Indian Astronomical Observatory (IAO), Hanle, using the HESP (high-resolution fiber-fed Hanle Echelle Spectrograph (HESP)) attached to 2m HCT (Himalayan Chandra Telescope). We have acquired two frames with exposure 2700s each. The spectra are combined to get the final spectrum with high S/N ratio. The spectrum covers from 3530 to 9970 Å in the wavelength range.

The spectrograph permits a resolution of 30,000 without slicer, and a resolution of 60,000 with slicer. The spectrum is recorded on a CCD with 4096×4096 pixels, each pixel of 15 micron size. The data reduction is performed following the standard procedures using spectroscopic data reduction packages of IRAF<sup>1</sup>. Basic data of the

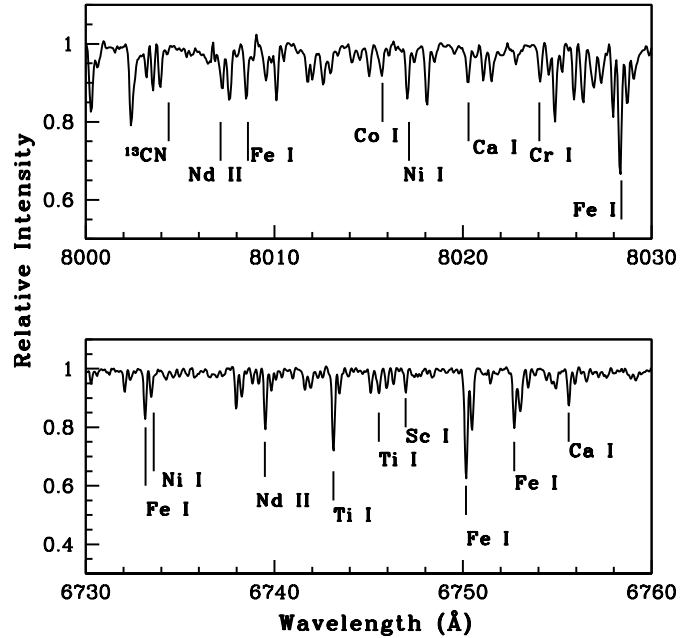


**Figure 1.** Examples of sample spectra of J045. The wavelength region 8000 to 8030 Å is shown in the Upper panel and the region 6730 to 6760 Å is shown in the Lower panel.

programme star is presented in Table 1. Examples of sample spectra of J045 are shown in Figure 1.

## 3 RADIAL VELOCITY AND STELLAR ATMOSPHERIC PARAMETERS

Radial velocity of J045 is calculated from the shift in the observed wavelength from the lab wavelength for clean and unblended lines and is found to be  $-65.1 \pm 0.05$  km s<sup>-1</sup> (Table 2). Jönsson et al. (2020) estimated a radial velocity of  $\sim -39.9$  km s<sup>-1</sup> for this object comparing its stellar spectrum with a grid of synthetic spectra. The estimated radial velocity of the object obtained using the LAMOST 1D pipeline by Luo et al. (2015) is  $\sim -70.1$  km s<sup>-1</sup>. Our estimate of radial velocity ( $-65.1$  km s<sup>-1</sup>) derived using several clean unblended lines on the spectra of this object is distinctly different from the estimate of Jönsson et al. (2020) and closer to the estimate of Luo et al. (2015). The difference in the estimates of radial velocity indicates that the object could possibly be in a binary system.

Atmospheric parameters, the effective temperature  $T_{\text{eff}}$ , surface gravity,  $\log g$  and microturbulent velocity  $\zeta$  of J045 are estimated using the equivalent widths measured for unblended and clean lines of Fe I and Fe II lines (Table A1). We have made use of thirty four Fe I and two Fe II lines for our analysis. The line information are taken

which is operated by the Association for Universities for Research in Astronomy, Inc., under contract to the National Science Foundation

<sup>1</sup> IRAF is distributed by the National Optical Astronomical Observatories,

**Table 1. LAMOST J045019.27+394758.7: Basic data**

RA(2000)	Dec.(2000)	Parallax (mas)	G <sup>a</sup>	J <sup>b</sup>	H <sup>b</sup>	K <sup>b</sup>	Exposure (seconds)	S/N (at 4750 Å)	(at 6000 Å)	Date of obs.
04 50 19.27	39 47 58.74	0.08±0.02	14.63	12.19	11.46	11.26	2700(2)	57	72	29-09-2018

*Note.* The number in the parenthesis with exposures indicates the number of frames taken, <sup>a</sup> Taken from SIMBAD Gaia DR2, <sup>b</sup> 2MASS, Cutri et al. (2003), The Naval Observatory Merged Astrometric Dataset (NOMAD) gives B and V magnitude of the object as 16.31 and 14.89 respectively with an error of ± 4.0 magnitude.

**Table 2. Radial velocities of the programme star.**

Star	V <sub>r</sub> (km s <sup>-1</sup> )	Reference
LAMOST J045019.27+394758.7	-65.1±0.05	1
	-70.1	2
	-39.9±0.01	3

1. Our work, 2. Luo et al. (2015), 3. Jönsson et al. (2020)

from linemake<sup>2</sup> (Placco et al. 2021), an atomic and molecular line database.

The effective temperature is fixed at the value by an iterative process for which the trend between the abundances derived using Fe I lines and the excitation potentials corresponding to those lines gives a slope close to zero. At this temperature, microturbulent velocity is adopted to be that value for which the Fe I lines abundances and the reduced equivalent widths do not exhibit any trends. At these values of effective temperature and microturbulent velocity, the surface gravity log g is fixed at the value, for which the abundances of Fe I and Fe II are nearly the same. The iron abundances of J045 as a function of excitation potential and as a function of equivalent widths are shown in Figure 2. The detailed procedure followed can be found in our earlier papers Purandardas et al. (2019b); Shejeelammal et al. (2021). We used MOOG (Sneden 1973, updated version 2013) for our analysis considering local thermodynamic equilibrium. We have selected the model atmospheres from the Kurucz grid of model atmospheres with no convective overshooting (<http://kurucz.harvard.edu/grids.html>). Solar abundances are taken from Asplund et al. (2009). The derived atmospheric parameters for J045 are presented in Table 3.

### 3.1 Mass and age

We could determine the mass and the age of J045 from its location on the H-R diagram, log(L/L<sub>⊙</sub>) vs. T<sub>eff</sub> (Figure 3). Luminosity of the star is determined using the relation,

$$\log(L/L_{\odot}) = (M_{\odot} - M_{bol})/2.5$$

Here M<sub>⊙</sub> represents the Sun's bolometric magnitude, and

$$M_{bol} = Mv + BC - Av$$

. Mv is determined using the equation,

$$Mv = V - (5 \log(d)) + 5$$

<sup>2</sup> linemake contains laboratory atomic data (transition probabilities, hyperfine and isotopic substructures) published by the Wisconsin Atomic Physics and the Old Dominion Molecular Physics groups. These lists and accompanying line list assembly software have been developed by C. Sneden and are curated by V. Placco at <https://github.com/vmplacco/linemake>.

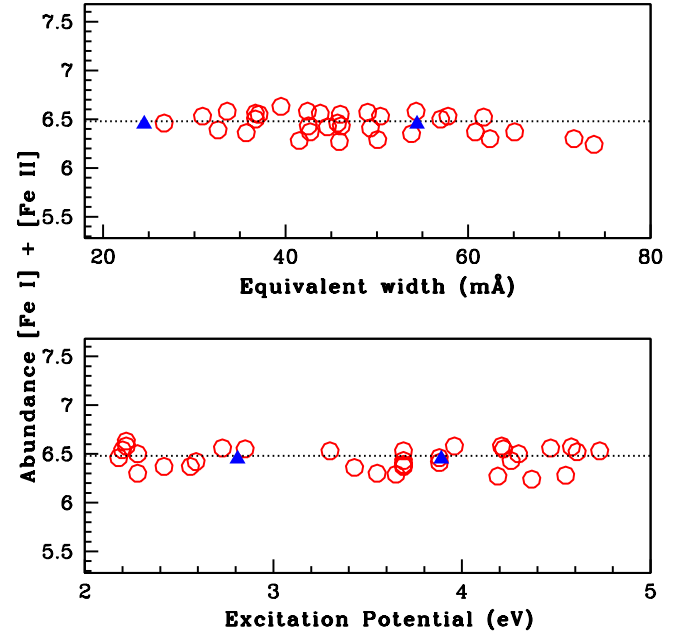


**Figure 2.** The iron abundances of J045 are plotted as a function of equivalent widths (upper panel) and excitation potential (lower panel). The open circles and the solid triangles represent the derived abundance estimates for Fe I and Fe II lines respectively.

The visual magnitude V of the star is adopted from the Naval Observatory Merged Astrometric Dataset (NOMAD) and the parallax values are adopted from Gaia (Gaia Collaboration et al. 2016, 2018, <https://gea.esac.esa.int/archive/>). Bolometric corrections are estimated using the empirical calibrations of Alonso et al. (1999). Instellar extinction used for the determination of bolometric magnitude is estimated from the formula given in Chen et al. (1998). We have used the evolutionary tracks and the isochrones from Girardi et al. (2000) corresponding to Z = 0.004 to determine the mass and the age of the star. From the location of J045 on the H-R diagram, we find that the object lies on the giant branch

**Table 3.** LAMOST J045019.27+394758.7: Derived atmospheric parameters and literature values.

$T_{eff}$ (K) ( $\pm 100$ )	$\log g$ cgs ( $\pm 0.2$ )	$\zeta$ ( $\text{km s}^{-1}$ ) ( $\pm 0.2$ )	[Fe I/H]	[Fe II/H]	[Fe/H]	$M_{bol}$	$\log(L/L_{\odot})$	Mass( $M_{\odot}$ )	$\log g$ (Parallax method) (cgs)	Age Gyr	Reference
4850	2.50	0.75	$-1.05 \pm 0.11$ (34)	$-1.05 \pm 0.00$ (2)	-1.05	$-0.92 \pm 0.55$	$2.27 \pm 0.22$	$2.00 \pm 0.50$	$2.17 \pm 0.10$	$0.79 \pm 0.49$	1
4627	2.26	0.72			-0.90						2
4250	1.00	1.55			-0.50						3

1. Our work, 2. [Xiang et al. \(2019\)](#)), 3. [Jönsson et al. \(2020\)](#)

with a mass  $\sim 2 M_{\odot}$ . The estimated age of the object J045 is 0.79 Gyr. Estimates of the mass and the age from the parallax method are tabulated in Table 3.

### 3.2 $\log g$ from parallax method

The surface gravity  $\log g$  of the object J045 is derived adopting our mass estimate in the relation

$$\log(g/g_{\odot}) = \log(M/M_{\odot}) + 4\log(T_{eff}/T_{eff\odot}) + 0.4(M_{bol} - M_{bol\odot})$$

The adopted Solar parameters  $\log g_{\odot} = 4.44$ ,  $T_{eff\odot} = 5770\text{K}$ , and  $M_{bol\odot} = 4.75$  mag are taken from [Yang et al. \(2016\)](#). The value of  $\log g$  estimated using the parallax method is  $2.17 \pm 0.10$  cgs, which is slightly lower than the estimated spectroscopic  $\log g$  value. However, we have used the estimated spectroscopic  $\log g$  value throughout our analysis.

## 4 DETERMINATION OF ELEMENTAL ABUNDANCES

Elemental abundances are estimated from the equivalent widths measured for a number of good lines due to various elements. We have also performed spectrum synthesis calculations whenever found applicable. Various lines are identified from the overplot of the Arcturus spectrum on the spectrum of J045. A master line list was generated including the equivalent width measurements, lower excitation potential of the lines and  $\log gf$  values obtained using linemake.

We have used only clean and symmetric lines for the measurement of equivalent widths. We could estimate the abundances for 25 elements as presented in the Table 4. We have performed the spectrum synthesis calculation for the elements that show hyperfine splitting, such as, Sc, V, Mn, Co, Ba, La, and Eu.

In the Table 4, we have presented the abundance results. The lines used for the determination of elemental abundances are tabulated in Table A2. Before presenting our discussion on elemental abundances, we present in the following, a discussion on verification of abundance estimates.

### 4.1 Verification of abundance estimates

In order to check how accurate our estimates are, we have performed an abundance analysis for the normal giant HD 111721 which has similar atmospheric parameters as that of J045. Two high-resolution spectra of this object, one from ELODIE (<http://atlas.obs-hp.fr/elodie/>) at a resolution of  $R \sim 42,000$  and one from the SUBARU Archive (<http://jvo.nao.ac.jp/portal/v2/>) at a resolution  $R \sim 50,000$ , are used for our analysis. The atmospheric parameters for HD 111721 ( $T_{eff} = 4947$  K,  $\log g = 2.63$ ,  $[\text{Fe}/\text{H}] = -1.34$ ), are adopted from [Ishigaki et al. \(2012, 2013\)](#). Our estimated elemental abundances when compared with those derived by [Ishigaki et al.](#)

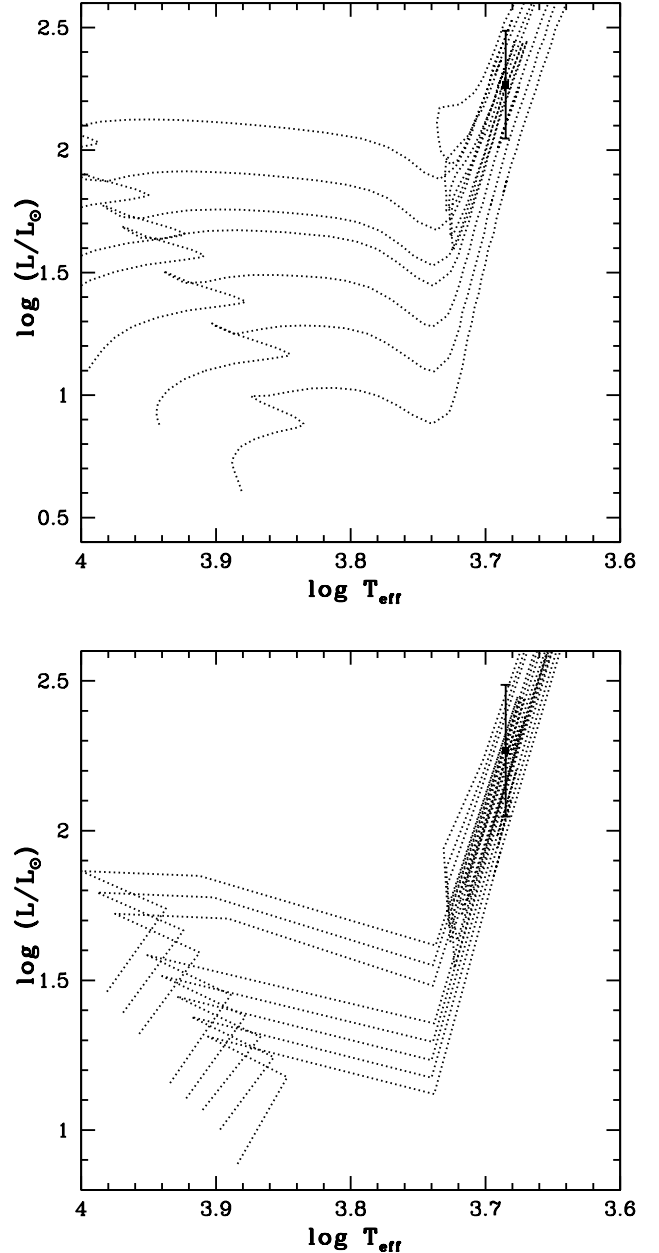


**Figure 3.** The location of J045 on the H-R diagram is shown. The evolutionary tracks for 1.3, 1.5, 1.7, 1.9, 2.0, 2.2, and 2.5  $M_{\odot}$  are shown in the upper panel from the bottom to top. The isochrones for  $\log(\text{age})$  9.25, 9.20, 9.15, 9.05, 8.95, 8.90, 8.85, and 8.80 are shown in the bottom panel from the bottom to top. The age of the programme star corresponds to the isochrone for  $\log(\text{age}) = 8.90$ .

**Table 4. Elemental abundances in LAMOST J045019.27+394758.7**

	Z	solar $\log \epsilon^*$	$\log \epsilon$	[X/H]	[X/Fe]
C (C <sub>2</sub> , 5165 Å)	6	8.43	7.49±0.20(syn)	-0.94	0.11
C (C <sub>2</sub> , 5635 Å)	6	8.43	7.49±0.20(syn)	-0.94	0.11
N	7	7.83	7.39±0.02(syn)	-0.44	0.61
O	8	8.69	7.51±0.20(syn)	-1.18	-0.13
Na I	11	6.24	5.87±0.11(3)	-0.37	0.68
Mg I	12	7.60	6.63±0.20(2)	-0.97	0.08
Si	14	7.51	6.64±0.05(7)	-0.87	0.18
Ca I	20	6.34	5.31±0.09(7)	-1.03	0.02
Sc II	21	3.15	1.82(3,syn)	-1.33	-0.28
Ti I	22	4.95	3.65±0.12(4)	-1.30	-0.25
Ti II	22	4.95	3.65±0.14(5)	-1.30	-0.25
V I	23	3.93	3.39±0.09(2,syn)	-0.54	0.51
Cr I	24	5.64	4.46±0.14(6)	-1.18	-0.13
Mn I	25	5.43	4.33±0.10(2,syn)	-1.10	-0.05
Fe I	26	7.50	6.45±0.11(34)	-1.05	-
Fe II	26	7.50	6.45(2)	-1.05	-
Co I	27	4.99	4.06±0.06(3,syn)	-0.93	0.12
Ni I	28	6.22	5.31±0.13(12)	-0.91	0.14
Zn I	30	4.56	2.89±0.11(2)	-1.67	-0.62
Sr I	38	2.87	1.92±0.20(1,syn)	-0.95	0.10 <sup>a</sup>
Y I	39	2.21	1.21(2,syn)	-1.00	0.05
Y II	39	2.21	1.28±0.14(2,syn)	-0.93	0.12
Ba II	56	2.18	1.04±0.04(2,syn)	-1.14	-0.09
La II	57	1.10	0.18±0.04(2,syn)	-0.92	0.13
Ce II	58	1.58	0.39±0.14(3)	-1.19	-0.14
Pr II	59	0.72	-0.23±0.04(2,syn)	-0.95	0.10
Nd II	60	1.42	0.20±0.08(2, syn)	-1.22	-0.17
Sm II	62	0.96	-0.10(2,syn)	-1.06	-0.01
Eu II	63	0.52	-0.24±0.11(2,syn)	-0.76	0.29

\* Asplund et al. (2009). The number of lines used for the abundance determination is given inside the parenthesis.

<sup>a</sup> After non-LTE correction

(2012, 2013) are found to be in close agreement (differences less than 0.05 dex) as shown in Table 5. This agreement confirms reliability of our abundance estimates and the line information used for the elemental abundance calculations.

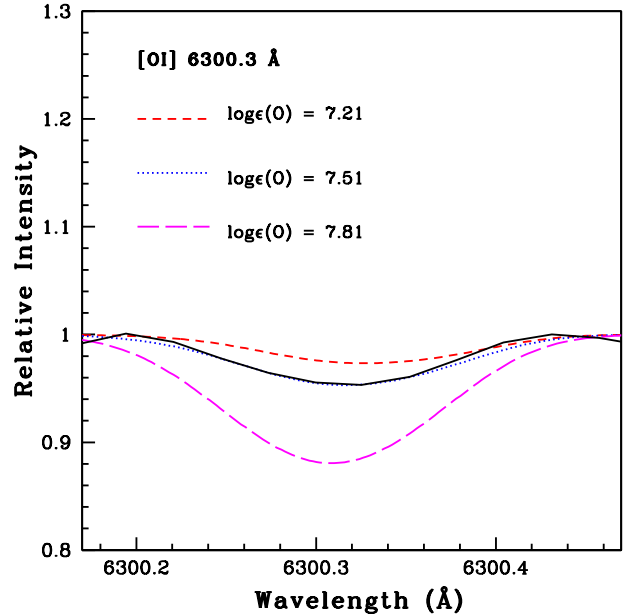
#### 4.2 O, C and N

Spectrum synthesis calculation of the oxygen forbidden line [OI] 6300.3 Å (Figure 4) is used to determine the oxygen abundance and is found to be marginally under-abundant with [O/Fe] ~ -0.13. We could not use the other lines of O such as [O I] 6363.7 Å and the oxygen triplets around 7774 Å as these lines are very weak and blended.

The [O I] forbidden line at 6300 Å is found to be influenced by Ni I blend. However, the effect of Ni I blend decreases and becomes negligible in stars with metallicity < -1 (Allende Prieto et al. 2001).

The spectrum synthesis of C<sub>2</sub> bands at 5165 and 5635 Å (Figure 5) is used to estimate the abundance of carbon which gives [C/Fe] ~ 0.11. We could not use CH band for the abundance determination of carbon as this region is very noisy. The spectrum synthesis of <sup>12</sup>CN lines at 8003, 8003.5 and 8004 Å are used for the estimation of nitrogen abundance. The three <sup>12</sup>CN lines give similar values for [N/Fe], 0.60, 0.63, and 0.59 respectively. The average [N/Fe] = 0.61 is listed in Table 4.

Using the estimated nitrogen and carbon abundances, we have determined the carbon isotopic ratio from the spectrum synthesis calculation of the CN band at 8005 Å (Figure 6). The estimated <sup>12</sup>C/<sup>13</sup>C ~ 52 and [C/N] = -0.50.

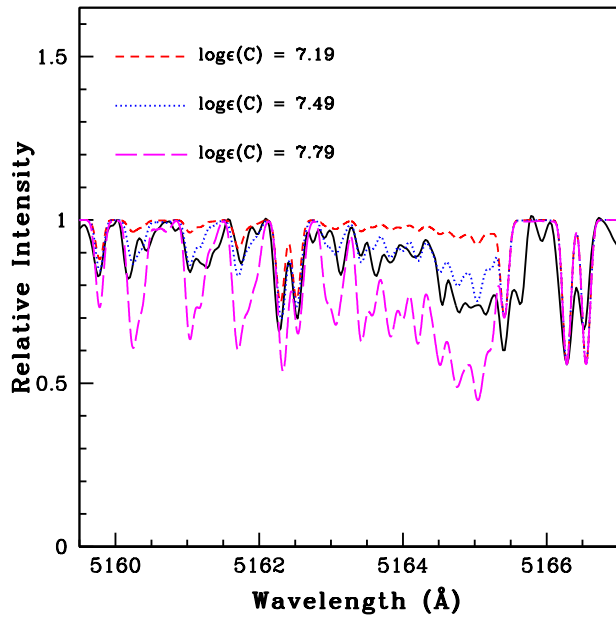


**Figure 4.** Synthesis of [OI] line around 6300 Å. Observed and synthesized spectra are represented by solid and dotted lines respectively. The Short-dashed line is used to represent the synthetic spectrum corresponding to  $\Delta[\text{O}/\text{Fe}] = -0.3$  and long-dashed line is used for  $\Delta[\text{O}/\text{Fe}] = +0.3$ .



**Table 5.** Comparison of the abundances of the star HD 111721 with the literature values.

Star name	[Na I/Fe]	[Mg I/Fe]	[Si I/Fe]	[Ca I/Fe]	[Sc II/Fe]	[Ti I/Fe]	[Ti II/Fe]	[V I/Fe]	[Cr I/Fe]	[Cr II/Fe]
HD 111721	0.00	0.40	0.34	0.31	0.20	0.28	0.40	-0.09	-0.14	0.17
	0.02	-	-	-	0.22	-	-	-	-0.16	0.18
	-	0.37	0.37	0.32	-	0.26	0.42	-0.06	-	-
	[Mn I/Fe]	[Ni I/Fe]	[Zn I/Fe]	[Y II/Fe]	[Ba II/Fe]	[La II/Fe]	[Nd II/Fe]	[Sm II/Fe]	[Eu II/Fe]	Ref
	-0.20	-0.07	0.17	0.11	0.21	0.26	0.19	0.28	0.23	1
	-0.20	-0.05	0.21	0.13	0.21	0.30	0.20	0.27	0.25	2
	-	-	-	-	-	-	-	-	-	3

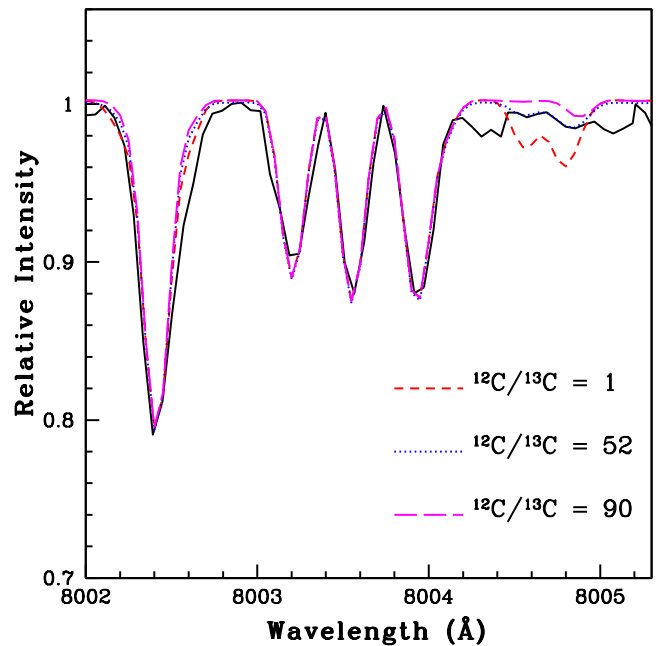
References : 1. Our work, 2. [Ishigaki et al. \(2013\)](#), 3. [Ishigaki et al. \(2012\)](#)**Figure 5.** Synthesis of C<sub>2</sub> band around 5165 Å. Observed and synthesized spectra are represented by solid and dotted lines respectively. The short-dashed line is used to represent the synthetic spectrum corresponding to  $\Delta[X/Fe] = -0.3$  and the long-dashed line for  $\Delta[X/Fe] = +0.3$ .

### 4.3 Odd-Z element Na

The equivalent widths of Na I lines at 5682.633, 6154.226, and 6160.7 Å are used for the estimation of Na abundance. Na is moderately enhanced in J045 with  $[Na/Fe] \sim 0.68$ .

### 4.4 Mg, Si, Ca, Sc, Ti, V

The equivalent widths of Mg I 4730.029, 5711.088 Å lines are used for the determination of Mg abundance which give an average value of  $[Mg/Fe] \sim 0.08$ . Silicon abundance is determined from the equivalent widths of seven Si I lines (Table A2) which gives a value of  $[Si/Fe] \sim 0.18$ . For the estimation of Ca abundance we have used a few Calcium I lines as presented in the Table A2 that give near-solar Ca abundance. The abundance of scandium is estimated from the spectrum synthesis calculations of Sc II 6245.637, 6309.920, 6604.601 Å lines which give an average value of  $[Sc/Fe] \sim -0.28$ . The equivalent widths of four Ti I and five Ti II lines (Table A2) are used for the estimation of Ti abundance. Our estimation shows

**Figure 6.** The spectral synthesis fits of CN band around 8005 Å are shown in this figure. The observed spectrum is represented by solid line. The dotted line represents the best fit synthetic spectrum corresponding to  $^{12}C/^{13}C = 52$ . The short- and the long-dashed lines illustrate the sensitivity of the line strengths to the isotopic carbon abundance ratios.

Ti is slightly under abundant with  $[Ti I, Ti II/Fe] \sim -0.25$ . Spectrum synthesis of V I lines at 5727.048 Å and 6251.827 Å give  $\log \epsilon(V)$  values as 3.32 and 3.45 respectively. In Table 4, an average value of  $[V/Fe] \sim 0.51$  is listed.

### 4.5 Cr, Mn, Co, Ni, Zn

The equivalent widths of a few Cr I lines (Table A2) are used to derive the Cr abundance. Cr is found to be marginally under-abundant with  $[Cr/Fe] \sim -0.13$ . Spectrum synthesis of the Mn I lines 6013.51, 6021.89 Å are used to estimate the abundance of Manganese which give an average value of  $[Mn/Fe] \sim -0.05$ . The spectrum synthesis calculations of Co I 5342.695, 5483.344, 6632.4 Å lines are used to determine the abundance of Co which is found to be marginally enhanced. Abundances of nickel and zinc are estimated using the equivalent widths measured for twelve Ni I lines and two Zn I lines 4722.2

Å and 4810.5 Å (Table A2). These two lines returned  $\log\epsilon(\text{Zn})$  values as 2.97 and 2.81 respectively. The average LTE abundance estimates give  $[\text{Zn}/\text{Fe}] = -0.62$ . The S/N (=57) ratio at 4750 Å is reasonably sufficient for reliable abundance measurements. While the abundance of Ni is found to be marginally enhanced, we find that the Zn is under abundant with  $[\text{Zn}/\text{Fe}] \sim -0.62$ . We have not applied non-LTE correction to the derived Zn abundance. The corrections for non-LTE effects on the two Zn lines used for abundance analysis are shown to be positive and relatively insignificant ( $< 0.1$  dex) in the range of metallicity  $-4.0 \leq [\text{Fe}/\text{H}] \leq 0$  (Takeda et al. 2005).

#### 4.6 Sr, Y, Zr

The abundances of strontium and yttrium in J045 are found to be close to the solar values. The spectral synthesis calculation of Sr I 4607.327 Å is used to derive the Sr abundance. We have applied the non-LTE correction to the estimated Sr abundance as given by Bergemann et al. (2012). For a star with  $T_{\text{eff}} = 4800$ ,  $\log g = 2.20$ , and  $[\text{Fe}/\text{H}] \sim -1.20$ , non-LTE correction is 0.32 (Bergemann et al. 2012). Figure 7 (left panel) shows the spectrum synthesis fits for the line Sr I 4607.3 Å. The abundance of yttrium is derived from the spectrum synthesis calculation of Y I 5630.130, 6435.004 Å lines and Y II 5119.112, 5402.774 Å lines. Due to the absence of good usable lines of zirconium in the spectrum of J045 we could not estimate Zr abundance.

#### 4.7 Ba, La, Ce, Pr, Nd, Sm, Eu

The estimated abundances of Ba, Pr, and Sm are found to be close to solar values. La is marginally enhanced, Ce and Nd are found to be marginally under-abundant, and Eu is only slightly enhanced. The spectrum syntheses of Ba II 5853.668, 6141.713 Å lines (Figure 7, right panel) return near-solar values with  $[\text{Ba}/\text{Fe}] \sim -0.09$ . Spectrum synthesis calculations of the lines La II 4921.776, 5303.528 Å are used to determine the abundance of lanthanum which give the value  $[\text{La}/\text{Fe}] \sim 0.13$ . Abundance of cerium is calculated using equivalent widths of three lines (Table A2) and is found to show the value  $[\text{Ce}/\text{Fe}] \sim -0.14$ . The spectral synthesis calculations of Pr II 5259.728, 6165.891 Å lines are used to find the Pr abundance and the spectral synthesis calculations of Nd II 4797.153, 5319.810 Å lines are used to determine the neodymium abundance. The estimated abundances of Pr and Nd are  $[\text{X}/\text{Fe}] \sim 0.10, -0.17$  respectively. The spectrum synthesis calculation of the lines Sm II 4566.200, 4676.9 Å give a value  $[\text{Sm}/\text{Fe}] \sim -0.01$ . The spectrum synthesis calculations of the lines Eu II 6437.640, 6645.064 Å return a slightly enhanced europium abundance with  $[\text{Eu}/\text{Fe}] \sim 0.29$ .

We have calculated the values of  $[\text{ls}/\text{Fe}]$ ,  $[\text{hs}/\text{Fe}]$ ,  $[\text{hs}/\text{ls}]$  ratios, where ls indicates Sr and Y the two light s-process elements, and the hs indicates Ba, La, Ce, and Nd, the heavy s-process elements. These values are presented in Table 6. A comparison between the estimated abundances of J045 and the literature values (whenever available) is presented in Table 7.

## 5 ABUNDANCE UNCERTAINTIES

Random and systematic errors produce uncertainties in the estimated elemental abundances. Random errors are caused by the uncertainties in the line parameters like equivalent widths, blending of lines and oscillator strength. The systematic error is produced due to the uncertainties in the stellar atmospheric parameters adopted for the analysis.

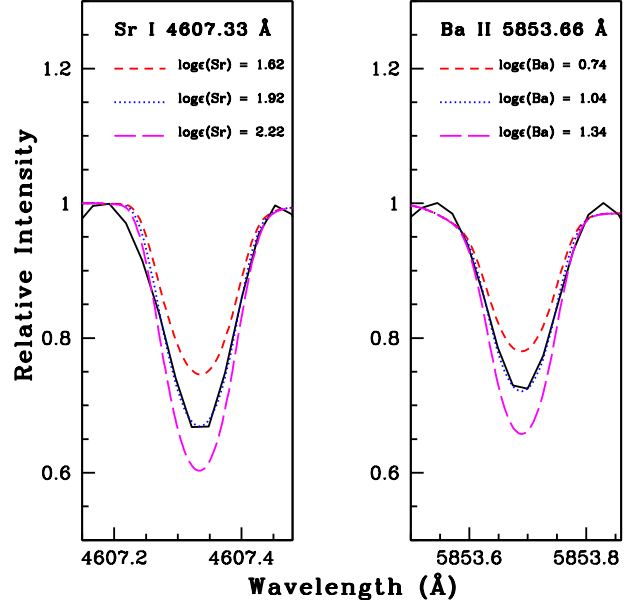


**Figure 7.** Spectral synthesis fits of the lines Sr I 4607.33 Å (left panel) and Ba II 5853.66 Å (right panel). The dotted lines represent synthesized spectra and solid lines indicate the observed spectra. The short-dashed lines represent the synthetic spectra corresponding to  $\Delta[X/\text{Fe}] = -0.3$  and the long-dashed lines correspond to  $\Delta[X/\text{Fe}] = +0.3$ .

We have calculated these uncertainties of our abundance estimates following the steps as discussed in Shejeelammal et al. (2021). The total uncertainties in the abundance estimates,  $\log\epsilon$  is given by

$$\sigma_{\log\epsilon}^2 = \sigma_{ran}^2 + \left(\frac{\partial \log\epsilon}{\partial T}\right)^2 \sigma_{T_{eff}}^2 + \left(\frac{\partial \log\epsilon}{\partial \log g}\right)^2 \sigma_{\log g}^2 + \left(\frac{\partial \log\epsilon}{\partial \zeta}\right)^2 \sigma_{\zeta}^2 + \left(\frac{\partial \log\epsilon}{\partial [\text{Fe}/\text{H}]}\right)^2 \sigma_{[\text{Fe}/\text{H}]}^2$$

where  $\sigma_{ran} = \sigma_s / \sqrt{N}$ .  $\sigma_s$  indicates the standard deviation in the abundance estimates which is calculated from the number of lines, N, corresponding to that particular element. The  $\sigma$ 's represent the uncertainties in the adopted atmospheric parameters of the star, and are given by  $T_{\text{eff}} \sim \pm 100$  K,  $\log g \sim \pm 0.2$  dex,  $\zeta \sim \pm 0.2$  km s<sup>-1</sup>, and  $[\text{Fe}/\text{H}] \sim \pm 0.1$  dex. The uncertainty in  $[\text{X}/\text{Fe}]$  is calculated using the relation :

$$\sigma_{[\text{X}/\text{Fe}]}^2 = \sigma_X^2 + \sigma_{[\text{Fe}/\text{H}]}^2$$

The differential elemental abundances obtained for J045 is presented in Table 8.

## 6 TESS PHOTOMETRY: SEARCH FOR VARIABILITY

We have used TESS photometric data to search for variability in J045. The Transiting Exoplanet Survey Satellite (TESS), the first high-precision full-sky photometry survey in space observed this LAMOST target (TIC 187263688) from September 28, 2019 to December 23, 2019, in sector 19 with Camera 1 CCD 3, exposure time of 1426s and 30-minute cadence. We acquired TESS Full Frame Images using Lightkurve (Lightkurve Collaboration et al. 2018) which utilizes the TESSCut tool (Brasseur et al. 2019). The target is near the limiting magnitude of TESS and the data is quite noisy. Since our target is quite faint, we have created appropriate aperture as shown in Figure 8. To account for the instrumental and noise effects, we have

**Table 6.** Estimates of [Fe/H], [ls/Fe], [hs/Fe], [hs/ls],  $^{12}\text{C}/^{13}\text{C}$  and [C/N]

Star name	[Fe/H]	[ls/Fe]	[hs/Fe]	[hs/ls]	$^{12}\text{C}/^{13}\text{C}$	[C/N]
LAMOST J045019.27+394758.7	-1.05	0.08	-0.07	-0.15	$52 \pm 3.0$	$-0.50 \pm 0.32$

**Table 7.** A comparison of the abundances of the programme star with literature values.

Star name	[Fe/H]	[C/Fe]	[N/Fe]	[O/Fe]	[Na/Fe]	[Mg/Fe]	[Si/Fe]	[Ca/Fe]	[Ti/Fe]
LAMOST J045019.27+394758.7	-1.05	0.11	0.61	-0.13	0.68	0.08	0.18	0.02	-0.25
	-0.90	0.47	0.47	-0.01	0.98	0.04	0.04	0.51	-0.06
	-0.50	0.54	0.18	0.04	0.15	0.10	0.04	0.09	-0.13
	[V/Fe]	[Cr/Fe]	[Mn/Fe]	[Co/Fe]	[Ni/Fe]	[Ba/Fe]	[Ce/Fe]	Ref	
	0.51	-0.13	-0.05	0.12	0.14	-0.09	-0.14	1	
	-	0.19	-0.21	-0.02	0.04	-0.44	-	2	
	-0.07	0.12	-0.17	-0.15	0.00	-	1.08	3	

References : 1. Our work, 2. Xiang et al. (2019), 3. Jönsson et al. (2020)

**Table 8.** Derived differential elemental abundances ( $\log \epsilon$ ) for the object LAMOST J045019.27+394758.7.

element	$\Delta T_{eff}$ ( $\pm 100\text{K}$ )	$\Delta \log g$ ( $\pm 0.2\text{dex}$ )	$\Delta \zeta$ ( $\pm 0.2\text{kms}^{-1}$ )	$\delta$ [Fe/H] ( $\pm 0.1$ dex)	$(\sum \sigma_i^2)^{1/2}$	$\sigma$ [X/Fe]
C	$\pm 0.02$	0.00	$\pm 0.01$	$\mp 0.01$	0.00	0.02
N	$\pm 0.29$	$\pm 0.05$	$\pm 0.04$	$\pm 0.13$	0.11	0.32
O	$\pm 0.02$	$\pm 0.08$	$\pm 0.02$	$\pm 0.03$	0.01	0.09
Na I	$\pm 0.07$	$\mp 0.01$	$\mp 0.02$	$\mp 0.01$	0.01	0.07
Mg I	$\pm 0.06$	$\pm 0.01$	$\pm 0.01$	$\pm 0.02$	0.00	0.06
Si	0.00	$\pm 0.02$	$\mp 0.01$	$\pm 0.01$	0.00	0.02
Ca I	$\pm 0.09$	$\mp 0.02$	$\mp 0.06$	$\mp 0.01$	0.01	0.11
Sc II	$\pm 0.01$	$\pm 0.09$	$\mp 0.01$	$\pm 0.05$	0.01	0.10
Ti I	$\pm 0.17$	0.00	$\mp 0.07$	$\mp 0.01$	0.03	0.18
Ti II	0.00	$\pm 0.08$	$\mp 0.02$	$\pm 0.03$	0.01	0.09
V I	$\pm 0.17$	0.00	$\mp 0.01$	$\mp 0.02$	0.03	0.17
Cr I	$\pm 0.14$	$\mp 0.01$	$\mp 0.09$	$\mp 0.01$	0.03	0.17
Fe I	$\pm 0.07$	$\pm 0.02$	$\mp 0.05$	$\pm 0.01$	0.01	
Fe II	$\mp 0.07$	$\pm 0.07$	$\mp 0.03$	$\pm 0.05$	0.01	
Mn I	$\pm 0.10$	$\mp 0.02$	$\mp 0.01$	$\mp 0.01$	0.01	0.10
Co I	$\pm 0.10$	$\mp 0.01$	0.00	$\mp 0.02$	0.01	0.10
Ni I	$\pm 0.09$	$\pm 0.02$	$\mp 0.04$	$\pm 0.01$	0.01	0.10
Zn I	$\mp 0.01$	$\pm 0.05$	$\mp 0.03$	$\pm 0.02$	0.00	0.06
Sr I	$\pm 0.24$	$\pm 0.01$	$\mp 0.03$	0.00	0.06	0.24
Y II	$\mp 0.05$	$\pm 0.02$	0.00	$\pm 0.01$	0.00	0.05
Ba II	$\mp 0.03$	$\mp 0.02$	$\mp 0.04$	$\mp 0.01$	0.00	0.05
La II	$\mp 0.04$	$\pm 0.10$	$\pm 0.02$	$\pm 0.08$	0.02	0.14
Ce II	$\pm 0.02$	$\pm 0.08$	$\mp 0.02$	$\pm 0.03$	0.01	0.09
Pr II	$\pm 0.03$	$\pm 0.08$	$\mp 0.01$	$\pm 0.03$	0.01	0.09
Nd II	$\pm 0.03$	$\pm 0.09$	$\mp 0.01$	$\pm 0.04$	0.01	0.10
Sm II	$\pm 0.01$	$\pm 0.10$	$\mp 0.04$	0.00	0.01	0.11
Eu II	$\pm 0.00$	$\pm 0.08$	$\mp 0.01$	$\pm 0.04$	0.01	0.09

applied regression correction to our light curve to remove trends, and set the light curve to the mean level. TESS scattered light is removed by subtracting model of the background that is built in Regression Correction. As seen from the Figure 9, we do not see any signatures of variability. Nonetheless, we employed Lomb-Scargle algorithm commonly used for detecting and characterising periodic signals in un-evenly sampled data (Lomb 1976; Scargle 1982). Lomb-Scargle periodogram is shown in Figure 9. The Lomb-Scargle algorithm performs computation of a Fourier-like power spectrum from un-evenly

sampled data allowing determination of the period of oscillation. No period of oscillation could be detected from the limited TESS data set.

## 7 KINEMATIC ANALYSIS

Kinematic analysis of J045 is performed following the detailed procedure as described in Purandardas & Goswami (2021b). The space



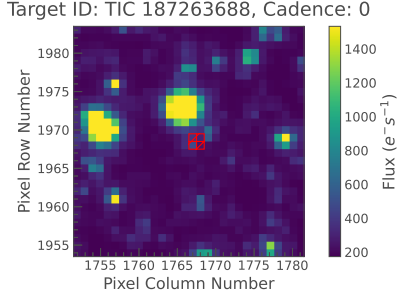


**Figure 8.** TESS Full Frame Image (FFI). The object location and the aperture used is shown in red.

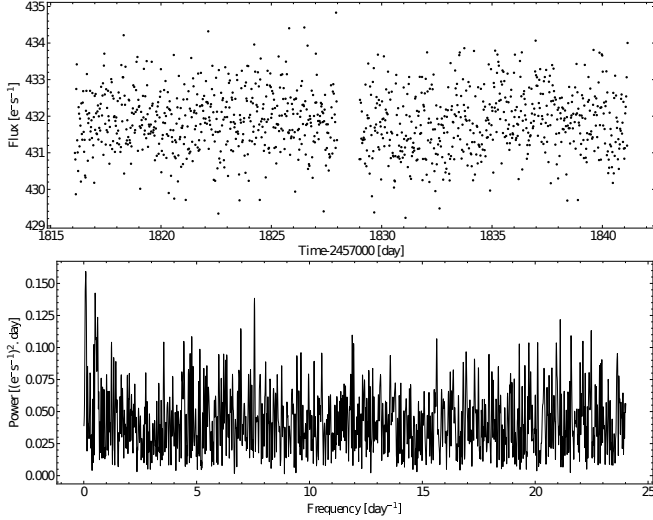


**Figure 9.** The regression corrected TESS light curves extracted from FFI (upper panel). Lomb-Scargle periodogram to check Fourier analysis of sinusoidal variations in the light curve (Bottom panel).

velocity is derived using a right-handed coordinate system. In this system,  $U$ ,  $V$  and  $W$  the three components of the space velocity are such that in the direction of the Galactic centre  $U$  is positive,  $V$  is positive in the direction of the Galactic rotation and  $W$  is positive in the direction of the North Galactic Pole (Johnson & Soderblom 1987). The values of parallax and proper motion of the star are taken from Gaia Collaboration et al. (2016, 2018) and we have used our estimate of radial velocity for the calculation.

We have also checked whether the programme star belongs to the thin disk, thick disk or the halo population. We have followed the procedures as discussed in Reddy et al. (2006); Bensby et al. (2003, 2004); Mishenina et al. (2004), and the assumption that the Galactic space velocity of the star has Gaussian distribution:

$$f(U, V, W) = K \times \exp\left[-\frac{U_{LSR}^2}{2\sigma_U^2} - \frac{(V_{LSR} - V_{asy})^2}{2\sigma_V^2} - \frac{W_{LSR}^2}{2\sigma_W^2}\right]$$

$$\text{Where } K = \frac{1}{(2\pi)^{\frac{3}{2}} \sigma_U \sigma_V \sigma_W}$$

The values for characteristic velocity dispersion  $\sigma_U$ ,  $\sigma_V$  and  $\sigma_W$  and the asymmetric drift  $V_{asy}$  are adopted from Reddy et al. (2006). We have presented the results of the kinematic analysis of the programme star in Table 9. Chen et al. (2004), have shown that the thin disk objects have spatial velocity  $< 85 \text{ km s}^{-1}$  and thick disk objects have spatial velocity in the range  $85 - 180 \text{ km s}^{-1}$ . Our estimated

space velocity  $\sim 78 \text{ km s}^{-1}$  therefore indicates that the object J045 to be a thin disk object. On the other hand, from high-resolution spectroscopic study of northern sky dwarf stars, Mikolaitis et al. (2019) have found that the stars with a lower combined velocity  $V_{spa} < 50 \text{ km s}^{-1}$  ( $V_{spa} = (U_{LSR} + V_{LSR} + W_{LSR})^{1/2}$ ) are most probably the thin-disk stars, whereas those with  $v_{spa} > 50 \text{ km s}^{-1}$  should belong to the thick-disk. Although following Mikolaitis et al. (2019)'s definition J045 is likely a thick disk object, if we consider the criteria that all stars with  $p_{thick}/p_{thin} > 2$  are thick-disk candidates and stars with  $p_{thick}/p_{thin} < 0.5$  are thin disk objects (Bensby et al. 2003, 2004), then, the J045 with  $p_{thick}/p_{thin} < 0.5$  seems to belong to thin-disk population.

## 8 ABUNDANCE ANALYSIS: DISCUSSION

The object J045 is included as a possible carbon star in LAMOST DR2 catalog, however, our detailed analysis shows that this object does not show any spectral characteristics of carbon stars and has a carbon abundance of near-solar value. The object is found to be a metal-poor giant with metallicity  $[\text{Fe}/\text{H}] \sim -1.05$  with unusual abundance for several key elements.

While the abundances of C is near-solar, N is found to be high with  $[\text{N}/\text{Fe}] = 0.61$ . One of the possible reasons for the observed enhancement of nitrogen in giant stars is the mixing which brings the CNO processed material to the surface that makes the atmosphere of the star "N rich" and "C poor" (Spite et al. 2005). However, as discussed below, the programme star does not show any signatures of mixing based on  $[\text{C}/\text{N}]$  and  $^{12}\text{C}/^{13}\text{C}$  ratios. However, if we consider the lower limit of error in  $[\text{C}/\text{N}]$  ratio, the star is well mixed. The origin of enhancement of nitrogen in a giant star can also be interpreted based on several scenarios. One such scenario is the accretion of N rich material from an AGB star (Lennon et al. 2003). However, the observed abundance patterns in the programme star does not support any AGB companion as the possible source of the nitrogen enhancement. Early accretion of Globular Clusters or dwarf spheroidal galaxies can also lead to nitrogen enhancement (Fernández-Trincado et al. 2019). This scenario makes the star chemically distinguishable from the stars that belongs to disk, halo, or bulge population. The dynamical history of such stars is not yet clearly understood (Fernández-Trincado et al. 2019).

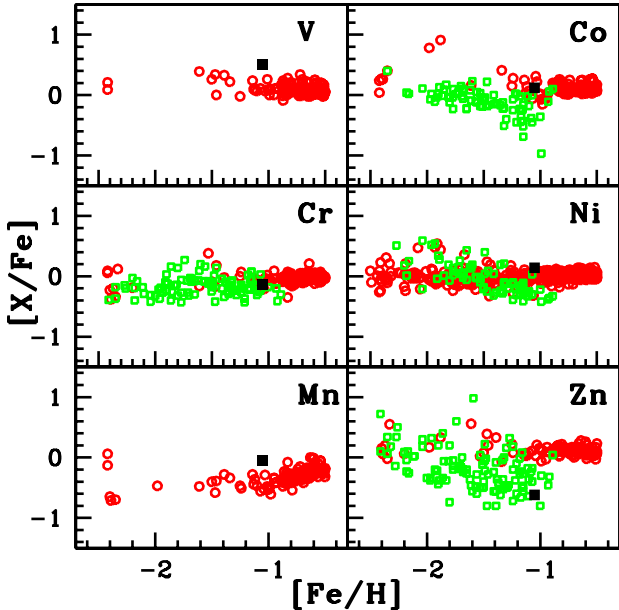
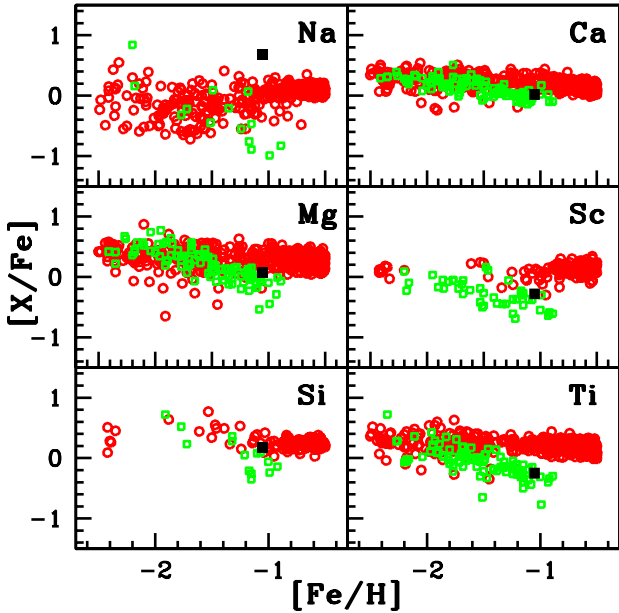
O is found to be marginally under-abundant with  $[\text{O}/\text{Fe}] \sim -0.13$ , a value which is highly unusual for a Galactic star of metallicity  $[\text{Fe}/\text{H}] \sim -1.0$ . None of the  $\alpha$ -elements Mg, Si and Ca are compatible with  $[\alpha/\text{Fe}]$  - enhancement (i.e., 0.3 to 0.4 dex) characteristic of Galactic metal-poor stars of similar metallicity. J045 shows almost solar values with  $[\text{Mg}/\text{Fe}] = 0.08$ ,  $[\text{Si}/\text{Fe}] = 0.18$ , and  $[\text{Ca}/\text{Fe}] = 0.02$ . Such abundance pattern is however compatible with stars of similar metallicity of Sculptor Dwarf Galaxy as shown in Figure 10 (upper panel). This comparison provides observational evidence to argue that the object could be a possible Dwarf Galaxy escapee in the Galaxy. Finding globular cluster (GC) escapees are not uncommon in the Galactic halo. While Martell et al. (2011) give an estimate of GC escapees in the halo to be  $\sim 3\%$ , an estimate of Dwarf galaxy escapees is not available in the literature.

Na is also enhanced with  $[\text{Na}/\text{Fe}] \sim 0.68$ . Such high abundance values for Na are generally not found to be reported for normal metal-poor Galactic stars of similar metallicity (Figure 11). Among the Dwarf Sculptor Galaxy stars one object UET0130 with a metallicity of  $-2.2$  is known to show very high Na abundance with  $[\text{Na}/\text{Fe}] = 0.84$  (Figure 12).

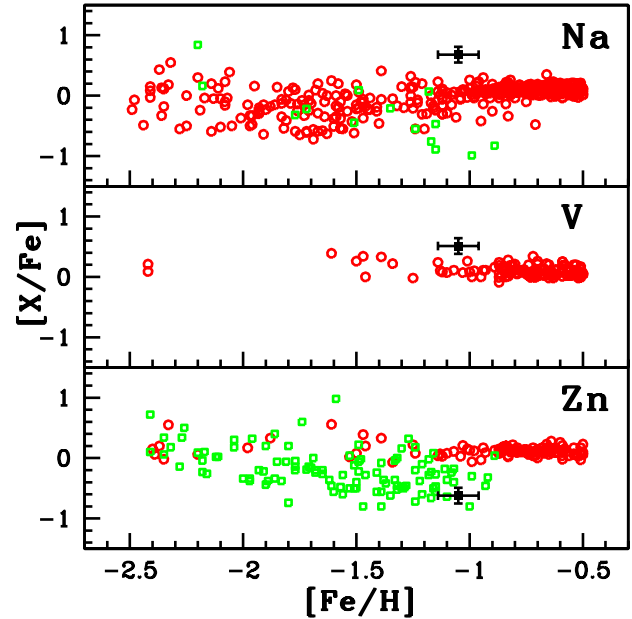
Among the Fe-peak elements, the Mn abundance is found to be

Table 9. Spatial velocity and probability estimates for the programme star

Star name	$U_{LSR}$ ( $\text{kms}^{-1}$ )	$V_{LSR}$ ( $\text{kms}^{-1}$ )	$W_{LSR}$ ( $\text{kms}^{-1}$ )	$V_{spa}$ ( $\text{kms}^{-1}$ )	$P_{thin}$	$P_{thick}$	$P_{halo}$	Population
LAMOST J045019.27+394758.7	$68.69 \pm 1.56$	$-29.92 \pm 6.90$	$-22.07 \pm 8.86$	$78.11 \pm 3.74$	0.94	0.05	0.00	Thin



**Figure 10.** A comparison of the light elements abundance ratios with their counterparts observed in Galactic stars and Sculptor dwarf galaxy stars. Comparisons are shown for elements for which literature data are available. Abundance ratios of elements with respect to metallicity estimated in J045 are represented using filled square in black colour. Red open circles represent Galactic normal giants from literature (Honda et al. 2004; Venn et al. 2004; Aoki et al. 2007; Luck & Heiter 2007; Hansen et al. 2016; Purandardas et al. 2019b). Sculptor dwarf galaxy stars from literature (Skúladóttir et al. 2017; Hill et al. 2019) are represented using green open squares.



**Figure 11.** Observed Na, V, and Zn abundance ratios of J045 (filled square) with respect to metallicity  $[\text{Fe}/\text{H}]$ . Red open circles are used to represent the Galactic normal giants from literature (Honda et al. 2004; Venn et al. 2004; Aoki et al. 2005, 2007; Reddy et al. 2006; Luck & Heiter 2007; Hansen et al. 2016; Yoon et al. 2016). Green open squares represent Sculptor dwarf galaxy stars from literature (Skúladóttir et al. 2017; Hill et al. 2019).

near-solar, whereas, Co and Ni are found to be marginally enhanced. Sc and Ti are found to be under-abundant with  $[\text{Sc}, \text{Ti}/\text{Fe}] \sim -0.28$  and  $-0.25$  respectively. As seen from Figure 10 (upper panel) these values match closely with Sculptor Dwarf Galaxy stars.

The  $[\alpha/\text{Fe}]$  ratios observed in J045 are generally noticed in dwarf spheroidal galaxies at closer metallicity (Koch & McWilliam 2008; Kirby et al. 2009). The observed  $[\text{Sc}/\text{Fe}] \sim -0.28$  and  $[\text{Ti}/\text{Fe}] \sim -0.25$  in J045 are also seen as typical values in many Sculptor Dwarf Galaxy stars (Skúladóttir et al. 2017; Hill et al. 2019).

The abundance of V with  $[\text{V}/\text{Fe}] = 0.51$  is higher than generally noticed in metal-poor Galactic stars. In a recent work, Ou et al. (2020) have derived abundance of Vanadium from a sample of 255 metal-poor stars in the metallicity range  $-4.0 \leq [\text{Fe}/\text{H}] \leq -1.0$ , and found that  $[\text{V I}/\text{Fe}] = -0.10 \pm 0.01$  from 128 stars and  $[\text{V II}/\text{Fe}] = 0.13 \pm 0.01$  from 220 stars. The authors suspect this offset to be due to departures from LTE and recommend using  $[\text{V II}/\text{Fe II}]$  values which is enhanced relative to solar ratio. We could not compare our estimate of vanadium abundance with Sculptor Dwarf Galaxy stars as literature values are not available.

The derived abundance of Zn with  $[\text{Zn}/\text{Fe}] = -0.62$  is found to be very different from its counterparts observed in Galactic giants and halo stars of similar metallicity. If we take account of the Non-LTE correction ( $< 0.1$  dex) zinc abundance will slightly enhance but still remains distinctly different from the Galactic trend. Saito et al.

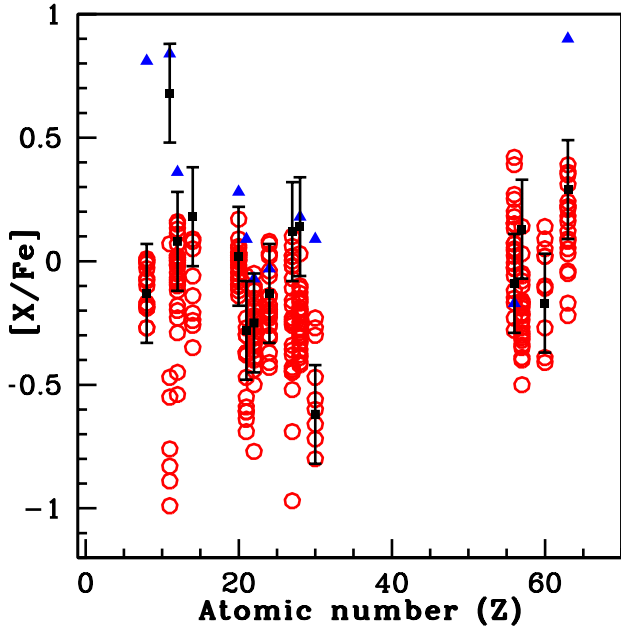


**Figure 12.** Comparison of observed elemental abundances of J045 (filled square) and the sculptor dwarf galaxy stars (red open circles) from literature (Skúladóttir et al. 2017; Hill et al. 2019). The elemental abundance ratios of the star UET0130 with  $[\text{Na}/\text{Fe}] \sim 0.84$  is shown in the plot with blue filled triangle.

(2009) studied the trend of  $[\text{Zn}/\text{Fe}]$  with respect to metallicity in the range  $-4.2 \leq [\text{Fe}/\text{H}] \leq +0.5$ , considering a large sample of stars (434 stars) belonging to the population of Galactic thin and thick disk as well as halo, and confirmed a trend where  $[\text{Zn}/\text{Fe}]$  decreases with increase of  $[\text{Fe}/\text{H}]$ .  $[\text{Zn}/\text{Fe}]$  was found to follow a nearly flat trend in the range of metallicity  $-2.0 \leq [\text{Fe}/\text{H}] \leq +0.5$ , with a slight enhancement of  $\sim +0.007$  dex upto  $[\text{Fe}/\text{H}] < -1.0$ . The enhancement was found to be more pronounced in the range  $-1.0 \leq [\text{Fe}/\text{H}] \leq -0.5$ , and the trend is found to gradually decrease to solar value in  $[\text{Fe}/\text{H}] > -0.5$ . This observed trend of  $[\text{Zn}/\text{Fe}]$  in the Galactic stars is very different from those observed in Sculptor Dwarf Galaxy (dSph) stars. As shown by Skúladóttir et al. (2017), the Sculptor Dwarf galaxy stars show a decreasing trend of  $[\text{Zn}/\text{Fe}]$  ratios at  $[\text{Fe}/\text{H}] > -1.8$  with a large star-to-star scatter ranging from  $-0.8$  to  $< 0.4$ . A comparison of the Zn abundance of J045 with the counterparts in dSph stars with similar metallicities (Figure 11) have shown a reasonably good match indicating that J045 could be a possible Sculptor Dwarf Galaxy escapee.

According to Skúladóttir et al. (2017), the  $[\text{Zn}/\text{Fe}]$  trend in the metallicity range  $-2.5 < [\text{Fe}/\text{H}] < -1.0$  observed in the Sculptor Dwarf galaxy stars can be attributed to SNe Ia that causes the slope of  $[\text{Zn}/\text{Fe}]$  to be steeper than that in a lower metallicity. Since SNe Ia is not able to produce Zn, stars formed out of a medium contaminated by the ejecta of SNe Ia are expected to show low  $[\text{Zn}/\text{Fe}]$  values and in particular, the stars with  $[\text{Zn}/\text{Fe}] < -0.5$  are believed to be formed from a medium which is predominantly influenced by the ejecta of SNe Ia.

Based on chemodynamical simulations of dwarf galaxies, Hirai et al. (2018) suggested that the electron-capture supernovae (ECSNe) can be one of the sources that can produce Zn as they could not justify the observed trends if ECSNe is not considered as a source of Zn.

The abundance of neutron-capture elements Sr, Y, Ba, Pr, Sm are

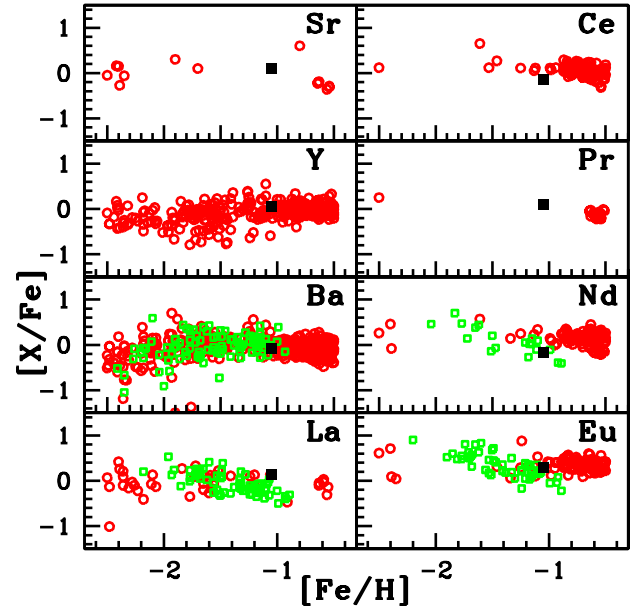


**Figure 13.** Same as Figure 10, but for heavy elements.

near-solar and La is marginally enhanced in J045. The abundance of Ce and Nd are marginally under-abundant, whereas Eu is mildly enhanced. In figures 10 and 13 we have compared the estimated abundance ratios of light and heavy elements in J045 with the corresponding ratios measured in normal Galactic giants and Sculptor dwarf galaxy stars. The observed abundance pattern in J045 is found to match well with that of Sculptor dwarf galaxy stars.

We have examined if the accretion of material from a binary companion could be a possible explanation for the non-typical abundance pattern observed in J045. The CH, CEMP-s, and CEMP-r/s stars are metal-poor stars that are believed to have been received gas transferred from an AGB companion. However, with an estimated  $[\text{C}/\text{Fe}] \sim 0.11$ , the star is neither carbon-enhanced nor s-process enhanced with  $[\text{X}/\text{Fe}] \sim$  solar values, where X stands for heavy elements.

### 8.1 Mixing diagnostic

Several mixing processes are found to occur in stars in their giant phase of evolution (Spite et al. 2006; Gratton et al. 2000). Since the object J045 is found to be a giant (Figure 3, upper panel), it is important to examine whether any internal mixing processes have altered the surface chemical composition of the star. The  $[\text{C}/\text{N}]$  and  $^{12}\text{C}/^{13}\text{C}$  ratios can give important clues regarding the occurrence of mixing. Spite et al. (2005) have shown that stars with  $[\text{C}/\text{N}] > -0.60$  and  $^{12}\text{C}/^{13}\text{C} > 10$  are unmixed stars. We have therefore checked for the signatures of any internal mixing based on the estimated  $[\text{C}/\text{N}]$  ratio and  $^{12}\text{C}/^{13}\text{C}$  ratios (Figures 14 and 15). Following the criteria of Spite et al. (2005), with  $[\text{C}/\text{N}] = -0.5$  and  $^{12}\text{C}/^{13}\text{C} = 52$  the star J045 does not seem to have undergone any internal mixing. When we consider the lower limit of the error ( $-0.32$ ) in  $[\text{C}/\text{N}]$  ratio, the program star is well mixed. But considering the upper limit of the error in  $[\text{C}/\text{N}]$  ratio, the program star remains unmixed. The estimated value of carbon isotopic ratio shows that the programme star is unmixed even within the error limits. The estimated high carbon isotopic ratio in J045 ( $\sim 52$ ) is not unusual. For example, Lucatello et al. (2003); Aoki et al. (2007); Purandardas et al. (2019a)

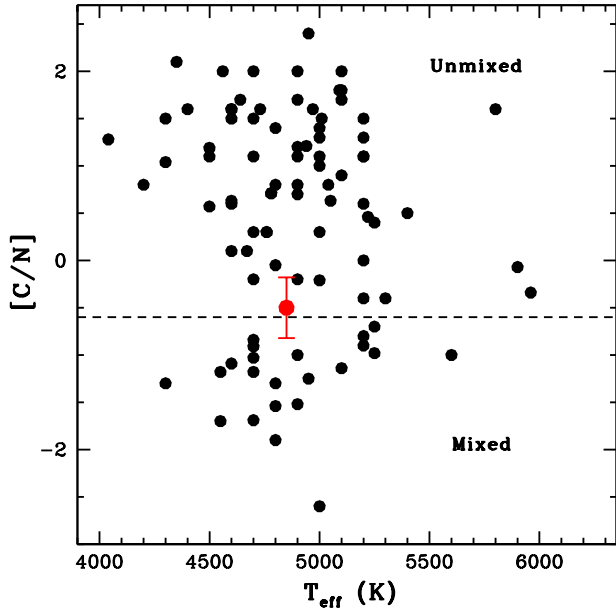


**Figure 14.** Position of J045 (Filled red circle) in the  $[C/N]$  vs.  $T_{\text{eff}}$  diagram. Filled black circles indicate the CEMP stars and the normal giants from literature (Spite et al. 2006; Aoki et al. 2007; Luck & Heiter 2007; Hansen et al. 2014; Goswami et al. 2016; Purandardas et al. 2019b,a; Goswami et al. 2021; Purandardas & Goswami 2021b,a; Shejeelammal et al. 2021; Shejeelammal & Goswami 2021). The dashed line at  $[C/N] = -0.6$  separates the two groups "Mixed" and "Unmixed". The location of J045 in this plot shows it to be "Unmixed", however, when the lower limit of error is considered the object falls into the "Mixed" group.

had reported  $^{12}C/^{13}C$  in the range 40 - 60 for giants of similar metallicity.

## 9 CONCLUSION

This work presents the results of a detailed spectroscopic analysis of the object J045 using high resolution spectra. The program star is presented in the list of possible carbon stars of LAMOST DR2 catalog. However, from our analysis we show that the program star does not show any spectral properties of a typical carbon star. From our analysis, we find that J045 is a metal-poor giant of metallicity  $[Fe/H] - 1.05$  with very unusual elemental abundances. The observed abundance pattern is not compatible with abundances characteristic of Galactic metal-poor stars of similar metallicity, but, matches quite closely with those observed in Sculptor Dwarf galaxy stars. This observational evidences prompted us to argue that J045 is likely a Sculptor Dwarf Galaxy escapee.

While the carbon abundance is estimated to be near-solar, N is over abundant with  $[N/Fe] \sim 0.61$ . Unlike in Galactic metal-poor stars, oxygen is found to be marginally under-abundant with  $[O/Fe] \sim -0.13$  and  $< [\alpha/Fe] > \sim 0.09$ . Na is found to be slightly enhanced with  $[Na/Fe] \sim 0.68$ . Sc and Ti are found to be under-abundant. While the Fe-peak element Mn is determined to be near-solar, Ni and Co are estimated to be marginally enhanced. Among the neutron-capture elements, Eu is marginally enhanced with  $[Eu/Fe] \sim 0.29$ . Sr, Y, Ba, Pr, and Sm show near-solar values. While La is marginally enhanced, Ce and Nd are found to be marginally under-abundant.

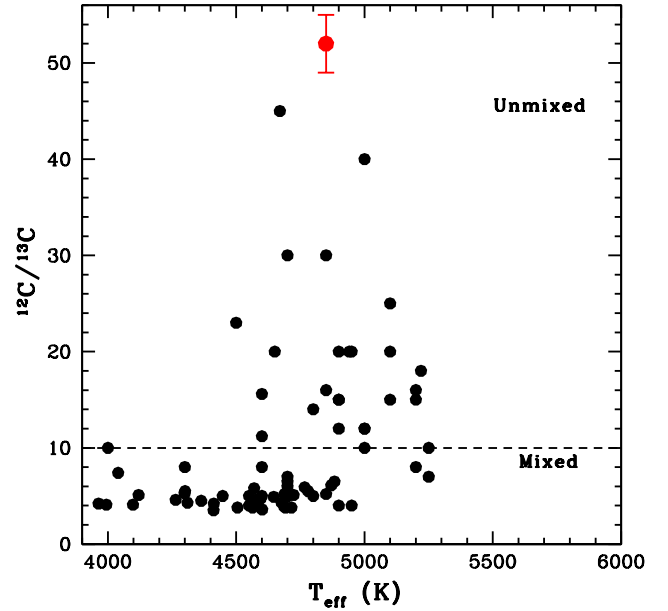


**Figure 15.** Position of J045 (Filled red circle) in the  $^{12}C/^{13}C$  vs.  $T_{\text{eff}}$  diagram. Filled black circles indicate the CEMP stars and normal giants from literature (Spite et al. 2006; Aoki et al. 2007; Maas et al. 2019). The dashed line at  $^{12}C/^{13}C = 10$  separates the groups "Mixed" and "Unmixed".

With the estimated  $[Ba/Eu] \sim -0.38$ , the star falls into the category of neutron-capture-rich star of r-I type of Beers & Christlieb (2005).

The estimated luminosity is high with  $\log(L/L_{\odot}) \sim 2.27$ . Such high values would indicate that the star might have undergone internal mixing. However, the estimates of  $[C/N]$  and  $^{12}C/^{13}C$  ratios show that the object has not undergone any significant internal mixing. We however note that, if we consider the lower limit of error in  $[C/N]$  ratio, the star is well mixed. From the kinematic analysis, we find that the program star is a thin disk object.

## ACKNOWLEDGEMENTS

We thank the referee Prof. Chris Sneden for his constructive and insightful comments that have significantly improved the manuscript. The facilities at IAO and CREST are operated by the Indian Institute of Astrophysics, Bangalore. We thank the staff members of IAO and CREST for help with observations. The DST SERB project EMR/2016/005283 is gratefully acknowledged. MP was a junior research fellow under this project. AG, DM, and SJ are grateful for the support received from the Indo-Thailand Programme of co-operation in Science and Technology through the Indo-Thai joint project DST/INT/Thai/P-16/2019. This work made use of the SIMBAD astronomical database, operated at CDS, Strasbourg, France, the NASA ADS, USA, and data from the European Space Agency (ESA) mission Gaia (<https://www.cosmos.esa.int/gaia>), processed by the Gaia Data Processing and Analysis Consortium (DPAC), (<https://www.cosmos.esa.int/web/gaia/dpac/consortium>). Based on data collected using HCT/HESP. Funding for the TESS mission is provided by NASA's Science Mission directorate.

## Data Availability



The data underlying this article will be shared on reasonable request to the corresponding author.

## REFERENCES

- Alksnis A., Balklavs A., Dzervitis U., Eglitis I., Paupers O., Pundure I., 2001, *Baltic Astronomy*, **10**, 1
- Allende Prieto C., Lambert D. L., Asplund M., 2001, *ApJ*, **556**, L63
- Alonso A., Arribas S., Martínez-Roger C., 1999, *A&AS*, **140**, 261
- Aoki W., et al., 2005, *ApJ*, **632**, 611
- Aoki W., Beers T. C., Christlieb N., Norris J. E., Ryan S. G., Tsangarides S., 2007, *ApJ*, **655**, 492
- Asplund M., Grevesse N., Sauval A. J., Scott P., 2009, *ARA&A*, **47**, 481
- Bai Y., et al., 2016, *Research in Astronomy and Astrophysics*, **16**, 107
- Beers T. C., Christlieb N., 2005, *ARA&A*, **43**, 531
- Bensby T., Feltzing S., Lundström I., 2003, *A&A*, **410**, 527
- Bensby T., Feltzing S., Lundström I., 2004, *A&A*, **415**, 155
- Bergemann M., Hansen C. J., Bautista M., Ruchti G., 2012, *A&A*, **546**, A90
- Brasseur C. E., Phillip C., Fleming S. W., Mullally S. E., White R. L., 2019, *Astrocut: Tools for creating cutouts of TESS images* (ascl:1905.007)
- Chen B., Vergely J. L., Valette B., Carraro G., 1998, *A&A*, **336**, 137
- Chen Y. Q., Nissen P. E., Zhao G., 2004, *A&A*, **425**, 697
- Christlieb N., Green P. J., Wisotzki L., Reimers D., 2001, *A&A*, **375**, 366
- Cutri R. M., et al., 2003, *VizieR Online Data Catalog*, p. II/246
- Fernández-Trincado J. G., et al., 2019, *A&A*, **631**, A97
- Gaia Collaboration et al., 2016, *A&A*, **595**, A1
- Gaia Collaboration et al., 2018, *A&A*, **616**, A11
- Gigoyan K. S., Hambaryan V. V., Azzopardi M., 1998, *Astrophysics*, **41**, 356
- Girardi L., Bressan A., Bertelli G., Chiosi C., 2000, *A&AS*, **141**, 371
- Goswami A., 2005, *MNRAS*, **359**, 531
- Goswami A., Aoki W., Beers T. C., Christlieb N., Norris J. E., Ryan S. G., Tsangarides S., 2006, *MNRAS*, **372**, 343
- Goswami A., Bama P., Shantikumar N. S., Devassy D., 2007, *Bulletin of the Astronomical Society of India*, **35**, 339
- Goswami A., Karinkuzhi D., Shantikumar N. S., 2010, *MNRAS*, **402**, 1111
- Goswami A., Aoki W., Karinkuzhi D., 2016, *MNRAS*, **455**, 402
- Goswami P. P., Rathour R. S., Goswami A., 2021, *A&A*, **649**, A49
- Gratton R. G., Sneden C., Carretta E., Bragaglia A., 2000, *A&A*, **354**, 169
- Hansen T., et al., 2014, *ApJ*, **787**, 162
- Hansen C. J., et al., 2016, *A&A*, **588**, A37
- Hill V., et al., 2019, *A&A*, **626**, A15
- Hirai Y., Saitoh T. R., Ishimaru Y., Wanajo S., 2018, *ApJ*, **855**, 63
- Honda S., Aoki W., Kajino T., Ando H., Beers T. C., Izumiura H., Sadakane K., Takada-Hidai M., 2004, *ApJ*, **607**, 474
- Ibata R., Lewis G. F., Irwin M., Totten E., Quinn T., 2001, *ApJ*, **551**, 294
- Ishigaki M. N., Chiba M., Aoki W., 2012, *ApJ*, **753**, 64
- Ishigaki M. N., Aoki W., Chiba M., 2013, *ApJ*, **771**, 67
- Ji W., Cui W., Liu C., Luo A., Zhao G., Zhang B., 2016, *ApJS*, **226**, 1
- Johnson D. R. H., Soderblom D. R., 1987, *AJ*, **93**, 864
- Jönsson H., et al., 2020, *AJ*, **160**, 120
- Kirby E. N., Guhathakurta P., Bolte M., Sneden C., Geha M. C., 2009, *ApJ*, **705**, 328
- Koch A., McWilliam A., 2008, *AJ*, **135**, 1551
- Lennon D. J., Dufton P. L., Crowley C., 2003, *A&A*, **398**, 455
- Lightkurve Collaboration et al., 2018, *Lightkurve: Kepler and TESS time series analysis in Python*, *Astrophysics Source Code Library* (ascl:1812.013)
- Lomb N. R., 1976, *Ap&SS*, **39**, 447
- Lucatello S., Gratton R., Cohen J. G., Beers T. C., Christlieb N., Carretta E., Ramírez S., 2003, *AJ*, **125**, 875
- Luck R. E., Heiter U., 2007, *AJ*, **133**, 2464
- Luo A. L., et al., 2015, *Research in Astronomy and Astrophysics*, **15**, 1095
- Maas Z. G., Gerber J. M., Deibel A., Pilachowski C. A., 2019, *ApJ*, **878**, 43
- Martell S. L., Smolinski J. P., Beers T. C., Grebel E. K., 2011, *A&A*, **534**, A136
- Mikolaitis Š., et al., 2019, *A&A*, **628**, A49
- Mishenina T. V., Soubiran C., Kovtyukh V. V., Korotin S. A., 2004, *A&A*, **418**, 551
- Ou X., Roederer I. U., Sneden C., Cowan J. J., Lawler J. E., Shectman S. A., Thompson I. B., 2020, *ApJ*, **900**, 106
- Placco V. M., Sneden C., Roederer I. U., Lawler J. E., Den Hartog E. A., Hejazi N., Maas Z., Bernath P., 2021, *Research Notes of the American Astronomical Society*, **5**, 92
- Purandardas M., Goswami A., 2021a, arXiv e-prints, p. arXiv:2108.06075
- Purandardas M., Goswami A., 2021b, *ApJ*, **912**, 74
- Purandardas M., Goswami A., Doddamani V. H., 2019a, *Bulletin de la Societe Royale des Sciences de Liege*, **88**, 207
- Purandardas M., Goswami A., Goswami P. P., Shejeelammal J., Masseron T., 2019b, *MNRAS*, **486**, 3266
- Reddy B. E., Lambert D. L., Allende Prieto C., 2006, *MNRAS*, **367**, 1329
- Saito Y.-J., Takada-Hidai M., Honda S., Takeda Y., 2009, *PASJ*, **61**, 549
- Scargle J. D., 1982, *ApJ*, **263**, 835
- Shejeelammal J., Goswami A., 2021, *ApJ*, **921**, 77
- Shejeelammal J., Goswami A., Shi J., 2021, *MNRAS*, **502**, 1008
- Skúladóttir Á., Tolstoy E., Salvadori S., Hill V., Pettini M., 2017, *A&A*, **606**, A71
- Sneden C. A., 1973, PhD thesis, THE UNIVERSITY OF TEXAS AT AUSTIN.
- Spite M., et al., 2005, *A&A*, **430**, 655
- Spite M., et al., 2006, *A&A*, **455**, 291
- Takeda Y., Hashimoto O., Taguchi H., Yoshioka K., Takada-Hidai M., Saito Y., Honda S., 2005, *PASJ*, **57**, 751
- Totten E. J., Irwin M. J., 1998, *MNRAS*, **294**, 1
- Venn K. A., Irwin M., Shetrone M. D., Tout C. A., Hill V., Tolstoy E., 2004, *AJ*, **128**, 1177
- Wu Y., et al., 2011, *Research in Astronomy and Astrophysics*, **11**, 924
- Xiang M., et al., 2019, *ApJS*, **245**, 34
- Yang G.-C., et al., 2016, *Research in Astronomy and Astrophysics*, **16**, 19
- Yoon J., et al., 2016, *ApJ*, **833**, 20

## APPENDIX A: LINE LISTS

Lines used for deriving elemental abundances.



**Table A1 :Equivalent widths (in mÅ) of Fe lines used for deriving atmospheric parameters.**

Wavelength(Å)	Element	$E_{low}$ (eV)	log gf	LAMOST J045019.27+394758.7
4438.350	Fe I	3.880	-1.630	26.7(6.46)
4446.830		3.690	-1.330	42.7(6.37)
4566.510		3.300	-2.250	30.9(6.53)
4635.850		2.850	-2.420	46.0(6.55)
4690.140		3.690	-1.640	32.6(6.39)
4768.320		3.690	-1.109	57.8(6.53)
4789.650		3.550	-0.910	62.4(6.30)
4907.740		3.430	-1.840	35.7(6.36)
4967.890		4.190	-0.622	45.9(6.27)
5079.220		2.200	-2.067	86.0(6.54)
5109.650		4.300	-0.980	36.7(6.50)
5369.960		4.370	0.350	73.8(6.24)
5373.700		4.470	-0.860	36.7(6.56)
5379.570		3.690	-1.480	42.5(6.43)
5543.940		4.220	-1.140	37.1(6.55)
5554.880		4.580	-0.440	49.0(6.57)
5618.630		4.210	-1.270	33.6(6.58)
5701.550		2.560	-2.216	65.1(6.37)
5753.120		4.260	-0.760	46.1(6.43)
5859.580		4.550	-0.398	41.5(6.28)
5883.810		3.960	-1.360	42.4(6.58)
5914.190		4.610	-0.050	61.7(6.52)
5956.690		0.860	-4.605	53.8(6.35)
6003.020		3.880	-1.120	49.3(6.41)
6082.710		2.220	-3.550	39.5(6.63)
6151.620		2.180	-3.299	45.7(6.46)
6180.200		2.730	-2.780	43.8(6.56)
6232.640		3.650	-1.270	50.1(6.29)
6240.650		2.220	-3.170	54.3(6.58)
6254.250		2.280	-2.400	71.6(6.30)
6419.940		4.730	-0.240	50.4(6.53)
6481.870		2.280	-2.984	57.0(6.50)
6575.020		2.590	-2.820	44.6(6.42)
6750.150		2.420	-2.620	60.8(6.37)
4520.220	Fe II	2.810	-2.600	54.4(6.45)
6247.557		3.892	-2.329	24.5(6.45)

The number in the parenthesis gives the derived abundance from the respective line.

Table A2: Equivalent widths (in mÅ) of lines used for deriving elemental abundances

Wavelength(Å)	Element	$E_{low}$ (eV)	log gf	LAMOST J045019.27+394758.7
5682.630	Na I	2.100	-0.700	89.6(5.99)
6154.230		2.100	-1.560	37.0(5.84)
6160.750		2.100	-1.260	49.3(5.78)
4730.030	Mg I	4.350	-2.523	31.6(6.77)
5711.090		4.350	-1.833	54.1(6.49)
5690.430	Si I	4.930	-1.870	25.9(6.68)
5772.150		5.080	-1.750	23.6(6.67)
5948.540		5.080	-1.230	42.8(6.59)
6131.850		5.620	-1.140	23.4(6.64)
6142.490		5.620	-1.480	19.1(6.87)
6155.140		5.620	-0.770	31.7(6.48)
6243.820		5.610	-1.100	21.5(6.55)
5261.710	Ca I	2.520	-0.730	55.1(5.26)
5581.970		2.520	-0.710	57.5(5.28)
5590.110		2.520	-0.710	58.8(5.31)
6166.440		2.520	-0.900	53.0(5.33)
6455.600		2.520	-1.350	41.7(5.50)
6471.660		2.530	-0.590	65.5(5.30)
6499.650		2.520	-0.590	62.6(5.23)
4453.710	Ti I	1.870	-0.010	26.7(3.73)
4759.270		2.250	0.514	32.9(3.78)
4840.870		0.900	-0.509	46.9(3.55)
5210.390		0.050	-0.884	72.0(3.53)
4568.310	Ti II	1.220	-2.650	25.6(3.57)
4764.530		1.240	-2.770	31.2(3.84)
4798.520		1.080	-2.430	46.6(3.72)
4865.610		1.120	-2.610	29.9(3.50)
5381.020		1.570	-2.080	34.9(3.59)
5737.060	V I	1.060	-0.740	41.6(3.76)
6039.720		1.060	-0.650	33.5(3.45)
6292.820		0.290	-1.470	48.4(3.66)
6531.420		1.220	-0.840	30.5(3.72)
4737.380	Cr I	3.090	-0.099	33.0(4.55)
4870.800		3.080	0.050	34.6(4.43)
4942.490		0.940	-2.294	43.8(4.50)
5247.570		0.960	-1.640	58.7(4.25)
5298.280		0.980	-1.150	79.3(4.38)
5300.740		0.980	-2.120	56.0(4.67)
4634.070	Cr II	4.070	-1.240	38.8(4.88)
4812.350		3.860	-1.140	40.1(4.59)
4703.800	Ni I	3.660	-0.735	33.6(5.16)
4732.460		4.110	-0.550	32.3(5.44)
4752.410		3.660	-0.700	45.0(5.44)
4852.560		3.540	-1.070	26.8(5.17)
4937.340		3.610	-0.390	49.2(5.18)
4953.200		3.740	-0.670	34.5(5.19)
6086.280		4.270	-0.530	28.5(5.45)
6111.070		4.090	-0.785	28.0(5.48)
6175.360		4.090	-0.530	33.9(5.39)
6186.710		4.110	-0.777	20.8(5.29)
6327.590		1.680	-3.150	41.3(5.33)
6643.640		1.680	-2.300	69.0(5.19)

The number in the parenthesis gives the derived abundance from the respective line.

Wavelength( $\text{\AA}$ )	Element	$E_{low}$ (eV)	log gf	LAMOST J045019.27+394758.7
4722.150	Zn I	4.030	-0.370	26.9(2.97)
4810.530		4.080	-0.150	27.3(2.81)
5119.110	Y II	0.990	-1.360	13.3(1.06)
5200.410		0.990	-0.570	37.7(1.07)
5402.770		1.840	-0.510	12.9(1.15)
4486.910	Ce II	0.290	-0.180	22.6(0.51)
4562.360		0.480	0.210	19.9(0.23)
4628.160		0.520	0.008	18.6(0.43)
5292.620	Pr II	0.650	-1.005	28.1(1.73)
6165.890		0.920	-0.205	18.9(0.90)
4451.560	Nd II	0.380	0.070	39.0(0.76)
4797.150		0.560	-0.690	19.4(0.98)
4811.340		0.060	-1.140	23.4(0.98)
4859.040		0.320	-0.440	32.8(0.90)
5130.590		1.300	0.450	29.3(1.03)
4434.320	Sm II	0.380	-0.070	14.8(-0.26)
4566.200		0.330	-0.590	11.4(0.04)
4674.590		0.180	-0.560	22.7(0.27)
4676.900		0.040	-0.870	11.7(-0.02)

The number in the parenthesis gives the derived abundance from the respective line.